Experimental Characterization of the Space Launch System Block 1B Liftoff and Transition Environment

Lee J. Mears[*], Patrick R. Shea[†], Jesse G. Collins[‡], Sarah L. Langston[‡], Morgan A. Walker[‡], and Jeremy T. Pinier[§]

NASA Langley Research Center, Hampton, VA, 23681

A wind tunnel test was conducted at the NASA Langley Research Center 14- by 22-Foot Subsonic Tunnel to evaluate the liftoff and transition flow environment of the Space Launch System Block 1B launch vehicles and tower interference effects with the newly designed Mobile Launcher 2. This test leveraged several unique diagnostic capabilities, including eight distributed force and moment measurements on the launch tower tiers, new umbilical and crew access arm configurations, and unsteady pressure acquisition on the rocket nose in the cargo configuration. The tower loading revealed a strong impact of the SLS vehicle height on force coefficients for individual tiers. Although the umbilicals produced weak influence on the loading on both vehicle and launch tower, unsteady pressure measurements revealed a slight increase in fundamental pressure oscillation frequency at specific wind azimuth directions. Multimodal flow states were observed in the gap flow between the vehicle and solid rocket boosters, producing different load profiles along the vehicle that are now incorporated in the vehicle database. This phenomenon was investigated using time-series measurements of forces as well as tufts and smoke flow visualization.

Nomenclature

C_A	Axial force coefficient, body axis
C_l	Rolling moment coefficient, body axis
C_m	Yawing moment coefficient, body axis
C_N	Normal force coefficient, body axis
C_n	Pitching moment coefficient, body axis
C_Y	Side force coefficient, body axis
D	SLS core diameter, ft
h	Launch vehicle elevation above launch platform, ft
h/L	Nondimensional launch vehicle elevation above launch platform
L	Launch tower height, ft
M_∞	Freestream Mach number
p_{rms}	Root-mean-squared fluctuating pressure, psf
q_∞	Freestream dynamic pressure, psf
r	Correlation coefficient
Re_D	Reynolds number based on core diameter
St_D	Strouhal number based on core diameter
α	Body axis angle of attack, degrees
β	Body axis sideslip angle, degrees
ψ_{azm}	Azimuthal angle on model surface, degrees
θ	Pressure port angle, degrees

[*]Research Engineer, Configuration Aerodynamics Branch, AIAA Member ✉ lee.j.mears@nasa.gov
[†]Research Engineer, Configuration Aerodynamics Branch, AIAA Senior Member
[‡]Research Engineer, Configuration Aerodynamics Branch, AIAA Member
[§]Research Engineer, Configuration Aerodynamics Branch, AIAA Associate Fellow

σ	Nondimensional fluctuating pressure, p_{rms}/q_∞
CAA	Crew Access Arm
CFD	Computational Fluid Dynamics
CUI	Controlled Unclassified Information
ESP	Electronic pressure scanner
EUS	Exploration Upper Stage
FRF	Frequency response function
LOT	Liftoff and Transition
ML-1	Mobile Launch tower for SLS Block 1
ML-2	Mobile Launch tower for SLS Block 1B
OML	Outer Mold Line
OSMU	Orion Service Module Umbilical
PSD	Power spectral density, psi^2/Hz
SLS	Space Launch System
SNR	Signal to Noise Ratio

Notice to the Reader

The Space Launch System, including its predicted performance and certain other features and characteristics, have been defined by the U.S. Government to be Controlled Unclassified Information (CUI). Information deemed to be CUI requires special protection and may not be disclosed to an international audience. To comply with CUI restrictions, details such as absolute values have been removed from some plots and figures in this paper. It is the opinion of the authors that despite these alterations, there is no loss of meaningful technical content. Analytical methodologies and capabilities are discussed; significant and interesting technical results are still present; and meaningful conclusions are presented.

I. Introduction

The National Aeronautics and Space Administration (NASA) continues to develop its heavy-lift launch vehicle, the Space Launch System (SLS), to achieve crewed deep-space exploration of our solar system. The SLS Block 1B (B1B) is the next iteration in vehicle design and capability (Fig. 1) and is planned to debut in the Artemis IV mission. A central core stage is powered by four RS-25 engines, which is supplemented for the first several minutes of flight by two Solid Rocket Boosters (SRBs). The Exploration Upper Stage (EUS) provides substantially greater thrust than the Interim Cryogenic Propulsion Stage (ICPS) used on SLS Block 1 missions, enabling greater payload capacity for lunar deep space missions. The liftoff and transition (LOT) flight environment experienced by the vehicle involves complex wake interactions with the launch tower, and extensive characterization of the forces and moments are essential for ensuring tower clearance and avoiding destructive aeroelastic conditions. Prior to liftoff, ground winds are the only aerodynamic forces on the vehicle. After engine ignition and liftoff, the vehicle transitions to forward flight and the effective angle of attack (considering the influence of ground winds) changes from α = 90° to 0°.

Extensive wind tunnel testing has been completed for Block 1 and 1B crew and cargo configurations of the launch vehicle, including measurements of forces, moments, and surface pressure [1–3]. To characterize the aerodynamic loading throughout the flight regime, wind tunnel tests and Computational Fluid Dynamics (CFD) simulations are performed for each condition, including assessing ground-wind loads in the liftoff configuration. The present wind tunnel test in the 14- by 22-Foot Subsonic Tunnel (14x22) provided the force and moments for the larger Block 1B Crew and Cargo vehicles with and without the newly designed Mobile Launch tower (ML-2). The test focused on building a database for steady (time-averaged) loads at low-speed conditions that the vehicle and launch tower will experience.

This test builds on the experience from four previous campaigns to characterize the LOT phase of flight in the 14x22 facility, beginning with the Ares I [4] and SLS Block 1 and B1B [1, 5] vehicles. Fidelity of the launch tower model has improved as the design has matured and the team has incorporated greater additive manufacturing capabilities, and a new B1B Cargo Outer Mold Line (OML) was implemented. This new design for the B1B Cargo vehicle incorporated a shallower nosecone angle that substantially increases the primary payload capacity volume.

This paper describes the LOT experiments conducted in May – June 2021 in the 14- by 22-Foot Subsonic Tunnel at the NASA Langley Research Center in Hampton, VA. The data collected in the test are used for multiple databases
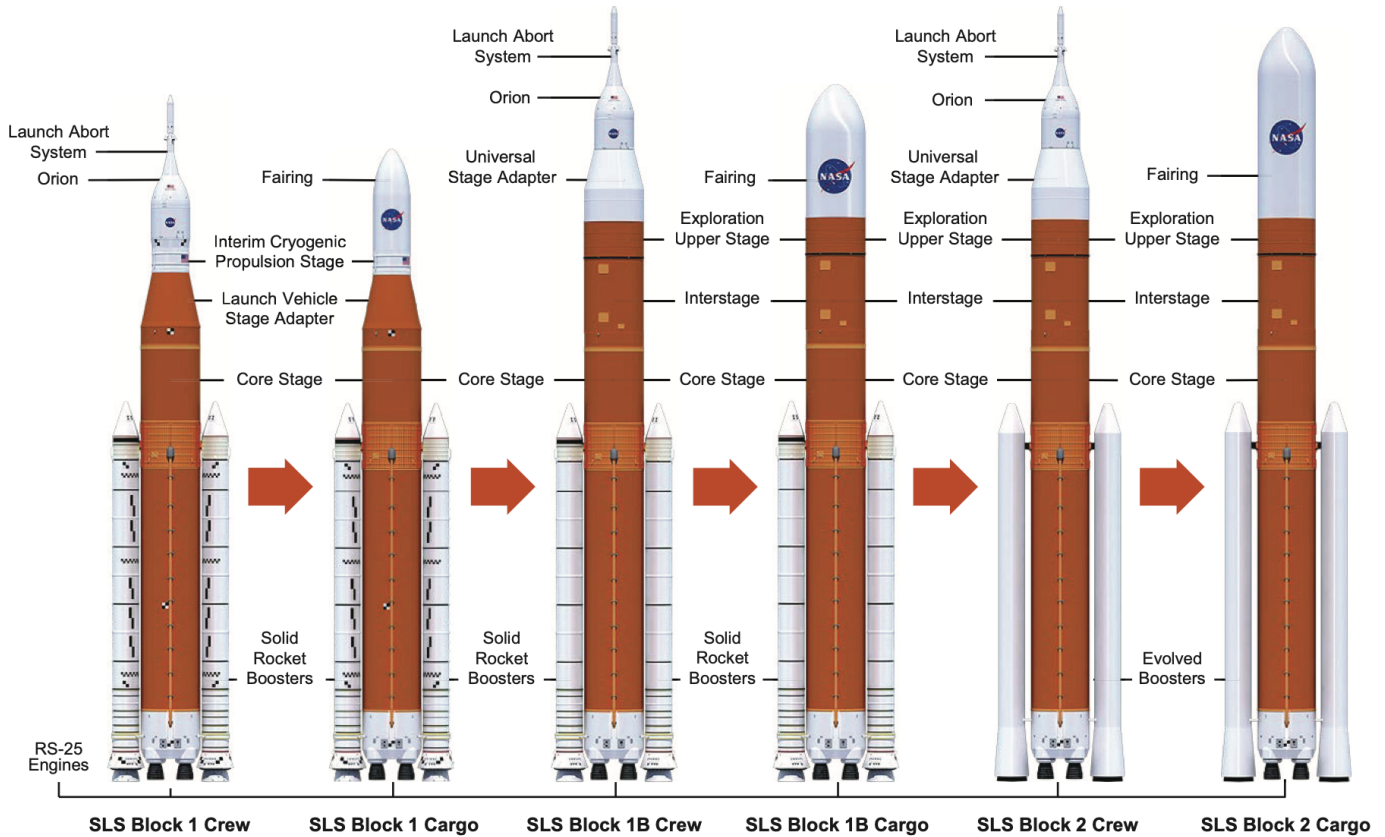
Fig. 1 NASA SLS configurations [6].

and groups in determining the safe flight environment, including booster loads, launch platform loading, and surface pressures used for CFD validation. This also presented an opportunity to acquire unsteady surface pressure data without significant additional investment in sensors or model alterations by leveraging a nonreimbursable Space Act Agreement between NASA and the University of Wyoming. Transition testing was conducted in a similar manner to previous tests, so the details of this paper will focus on the novel aspects of the liftoff test.

II. Experiment Setup

A. Facility

The test campaign was performed at the NASA Langley Research Center in the 14- by 22-Foot Subsonic Tunnel (14x22). This closed-circuit, atmospheric wind tunnel can operate in different test section configurations, and with the walls closed, the test section dimensions are 14.5 ft high by 21.75 ft wide by 50 ft long. An aerial photograph of the wind tunnel on the NASA Langley Research Center campus is shown in Fig. 2. The 12,000 horsepower drive motor spins the 40-foot-diameter fan to provide a continuous range of test section Mach numbers from 0 to 0.3. The flow in the settling chamber is conditioned by a flow-straightening honeycomb, four square-mesh screens with a mesh count of 10 per inch and 64% open area, and a tunnel contraction ratio of 9 to 1 to match the test section dimensions [7]. Previous studies have reported turbulence intensities near the center of the test section between 0.05-0.07% of the freestream velocity at a dynamic pressure (q_∞) of 50 psf [8].

Model support is installed on 14x22 Model Cart #2, which contains a turntable and vertical post mounting system with integrated pitch range of -10° to 50° with vertical motion from the tunnel floor to approximately the center of the test section. An additional pitch head assembly with 45° offset that was implemented in Test 633 [1] was reused in the current test to reach the full range of transition α of 0° to 90°. All runs were acquired using point-pause motion of the test article. Once pressure readings and force and moment readings have settled at a specified dynamic pressure and

vehicle orientation, acquisition is initiated. Temperature variations resulted in a range of Mach and Reynolds numbers during testing. For nominal q_∞ = 50 psf tests, the Mach number varied between 0.185 and 0.187. The dynamic pressure typically varies by 0.3% during data acquisition. Variations in outdoor temperature resulted in test section temperatures from 70°F to 105°F, resulting in unit Reynolds number ranging between 6.0×10^6 per foot and 6.2×10^6 per foot.

The wind tunnel has an option for boundary layer suction upstream of the test section, but the vehicle and ML-2 are mounted on a splitter plate in the liftoff configuration that provides 5 inches of clearance, which is greater than the expected boundary layer thickness at the model station. Results in the vehicle-alone configuration were consistent throughout the vertical range tested, which confirms that boundary layer influence is adequately mitigated by the splitter plate.

Fig. 2   Aerial view of the NASA Langley 14x22 Subsonic Tunnel [9].

B. SLS Block 1B Models

The 1.75%-scale model consists of two primary components: a centerbody core with an attached pair of solid rocket boosters (SRBs) – together comprising the SLS launch vehicle – and a mobile launch tower (ML-2) that provides support to the vehicle prior to liftoff. The two vehicles tested were the Block 1B crew (28005) and the newly redesigned Block 1B cargo (27007). Figure 3 depicts the B1B cargo launch vehicle in the liftoff configuration next to the ML-2 installed in the wind tunnel. The Block 1B crew vehicle was previously tested in 14x22 Test 633, and was reused in the current test to provide comparison data and to evaluate the tower interference using the higher-fidelity ML-2 model, rather than the simple tower extension added to the ML-1 in the previous test. The test-to-test comparison provides a comprehensive quality review for testing conditions, instrumentation, and data reduction. A previous version of the Block 1B cargo vehicle was also tested as part of Test 633 but became obsolete due to SLS design improvements since 2017, which required a new model to be fabricated. A larger payload fairing and updated protuberances, including several cameras, stabilizer brackets, fuel vents, and a systems tunnel for the upper stage are included in the vehicle OML. Both crew and cargo vehicles use the same core, so model changes involve replacing the nose section while the rest of the centerbody, which includes the balance, remains fixed.

The same internal balance (VST-15) that was used in Test 633 is installed in the SLS vehicle core to measure forces and moments on the full stack, including the centerbody and SRBs. A sting attaches the balance to the roll coupler during transition testing or to the vertical post during liftoff testing. At the forward and rear attachment between the centerbody and SRBs, two integrated ATI mini45 load cells are used to calculate combined force and moment measurements for each SRB. Details on the force and moment instrumentation, including definitions of the body and missile axis coordinate systems for the vehicle, are not included for brevity and are described by Chan [1].

To artificially replicate higher Reynolds number flow conditions, transition grit is used to transition the boundary layer from laminar to turbulent to better match conditions on the full scale vehicle. Distributed roughness (#80 grit
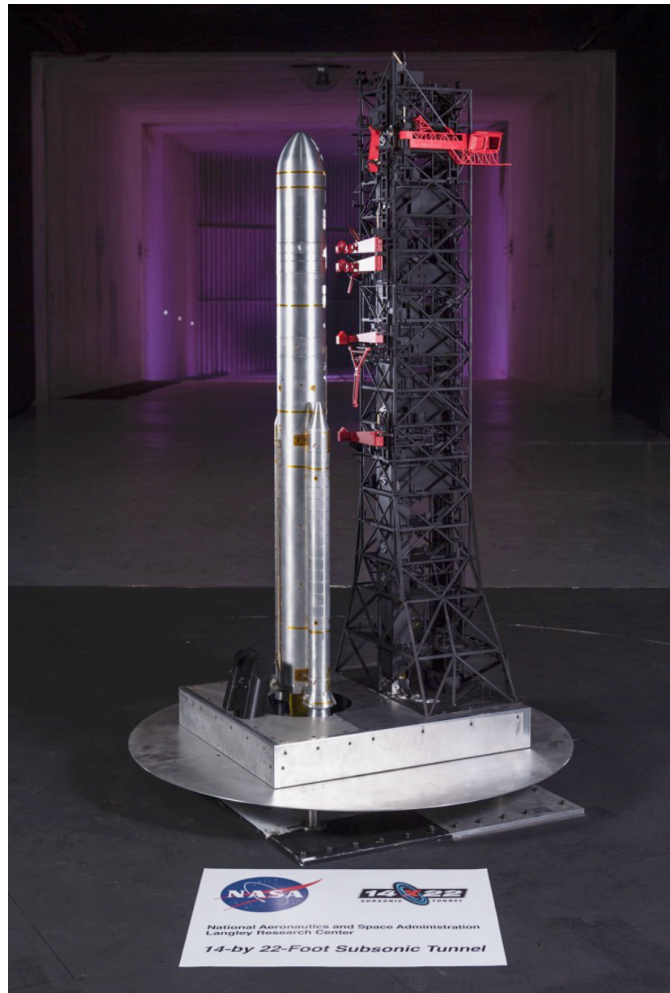
Fig. 3   SLS Block 1B Cargo 1.75%-scale model with ML-2 mobile launch tower installed in the test section of the Langley 14x22 Subsonic Tunnel.

carborundum) is adhered to the entire vehicle surface to promote boundary layer transition. Previous studies in LOT environment demonstrated that distributed surface grit produces more consistent results than discrete trip dots over the wide range of angles of attack (0° - 90°) tested [4].

C. ML-2 Launch Tower

Prior to launch, SLS vehicles will roll out along with a Mobile Launch Tower on top of crawler-transporter #2 from the NASA Kennedy Space Center Vehicle Assembly Building to Launch Pad 39B. Previous LOT tests used the ML-1, which will interface with Block 1 vehicles. Since the Block 1B vehicles are taller and the positions of the support umbilicals and Crew Access Arm (CAA) are higher than those on Block 1 vehicles, a taller tower is required. Several other differences include increased porosity in the ML-2 and an elevator shaft that is aligned with the center of the SLS vehicle, while the ML-1 featured an offset elevator shaft.

The new model design provided an opportunity to incorporate a long-standing desired measurement of distributed loads on separate tower sections, known as tiers. This design challenge was motivated by requests for higher resolution experimental data to validate CFD simulations of aerodynamic loads experienced by the tower structure. The approach and instrumentation used to implement the distributed loading measurements is described in Section IIIA.

D. Model Configurations

Three sequences of testing were conducted during the liftoff phase, each consisting of similar flow conditions with changes to the model configuration, shown in Fig. 4. The vehicle configurations in chronological order are as follows: ML-2 installed and umbilicals deployed (Fig. 4(a)); ML-2 installed and umbilicals retracted (Fig. 4(b)); and ML-2 removed or vehicle-alone (Fig. 4(c)). Umbilicals are support structures connecting the ML-2 and the launch vehicle that fall away from the vehicle shortly before liftoff, which are shown in red in Fig. 4(a) and (b). Umbilicals differ between crew and cargo variants since the Orion crew module is not included and no CAA or Orion Service Module Umbilical (OSMU) is required for cargo missions. Deployment of the umbilicals simply means that the parts are moved away from the tower and are positioned very close to the vehicle surface – in reality, the umbilicals attach to the launch vehicle, but for purposes of force and moment testing, a small clearance gap is maintained between the parts to avoid fouling. The ML-2 and ground plane are completely removed for the vehicle-alone configuration, as shown in Fig. 4(c).

The vehicle balance is mounted to a sting with motorized height adjustment relative to the launch tower, and tests were conducted at nominal height increments of $h/L = 0.1$ over a range of h/L = -0.003 to 0.876, where h equals the vertical elevation of the vehicle above the ML-2 and L is the height of the ML-1 launch tower, as shown in Fig. 5. Due to the selected reference point on the vehicle, h/L = -0.003 is the lowest height tested, where the SLS vehicle sits prior to liftoff. A previous test [1] used a half-tower model to simulate higher values of h/L, but the influence on vehicle forces and moments was minimal and the attainable elevation values with the full tower are sufficient for generating the required database.

In the liftoff configuration, the vehicle and launch tower are mounted on a yaw table in the liftoff configuration perpendicular to the wind tunnel floor. The vehicle angle of attack is 90° (vertical orientation) and the freestream flow simulates incoming ground winds. Figure 6 shows the definition of wind direction, ψ_{azm}, ranging from 0° to 360° with respect to the vehicle and ML-2. The cardinal directions correspond to the geographical orientation of Launch Pad 39B in Cape Canaveral, Florida, where the ML-2 lies directly north of the SLS vehicle. Tests were conducted using ψ_{azm} increments of 10°, resulting in 33 angles, since 80°, 90°, and 100° were unattainable (gray region in Fig. 6) due to mechanical constraints of the yaw table.

Although static pressure was measured at ports on both cargo and crew vehicles, one ring on the cargo vehicle was dedicated to measuring unsteady pressures using an ESP scanner and five Kulites connected to a Resono measurement system. The pressure ports are sequentially numbered from 1 to 12, and Ports 1, 4, 9, 10, and 11 have corresponding comparison Kulites (yellow triangles in Fig. 7). The data from each pressure port is plotted with respect to the incoming flow direction, ψ_{azm}, using a new variable, θ, shown in Fig. 7). Port position is oriented such that the nominal stagnation point is at $\theta = 0°$, and positive θ in the clockwise direction looking top-down to the model. Extensive details on the unsteady pressure instrumentation can be found in a recent report [10].

(a) Umbilicals deployed   (b) Umbilicals retracted   (c) Vehicle alone
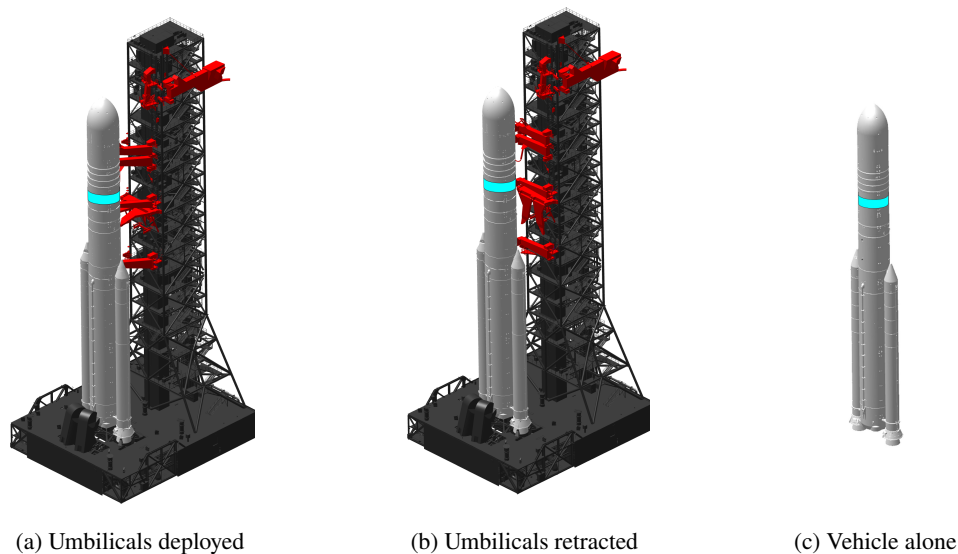
Fig. 4 Model configurations for SLS Block 1B vehicle and ML-2 representing the environment before and after liftoff. The cyan ring shows the approximate axial location of unsteady pressure measurement.
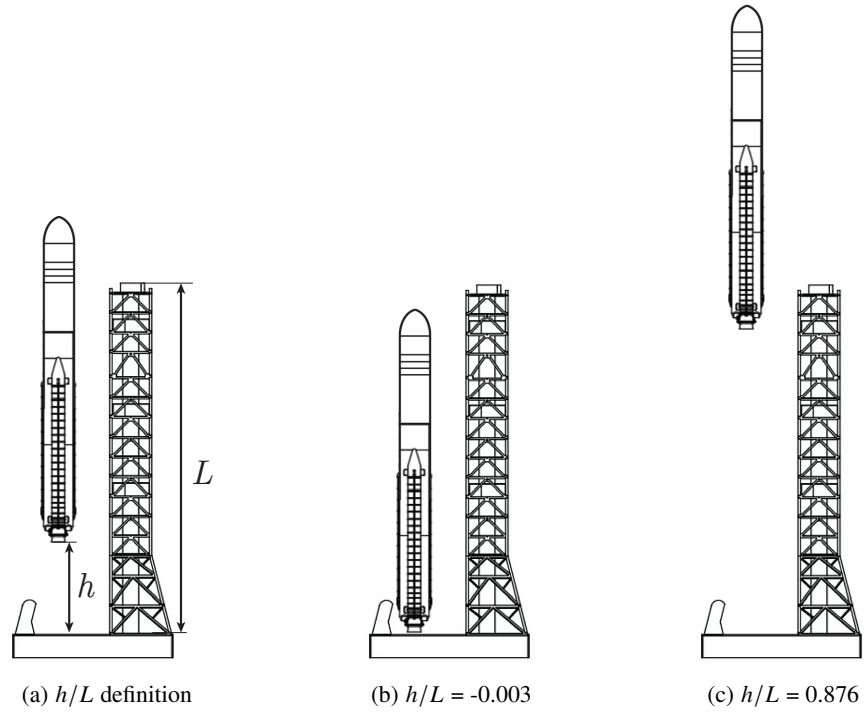
(a) h/L definition   (b) h/L = -0.003   (c) h/L = 0.876

Fig. 5   Launch vehicle elevation with respect to the launch tower height (h/L) and limiting cases in the present test campaign.
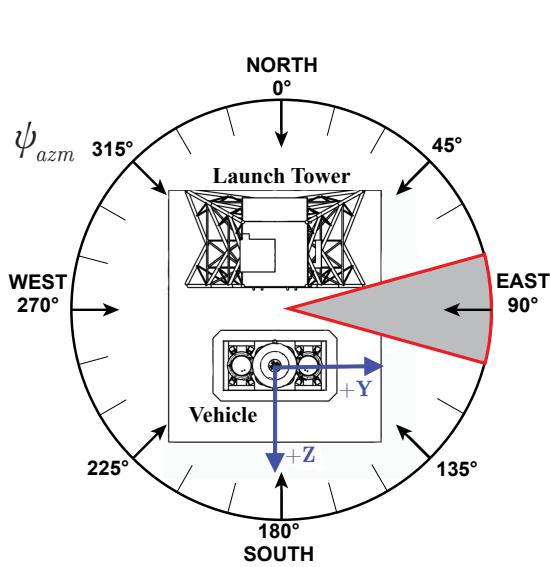

Fig. 6   Top-down view of the model with wind direction ψ_{azm} definition. Angles 80°-100° (gray sector) were not attainable.
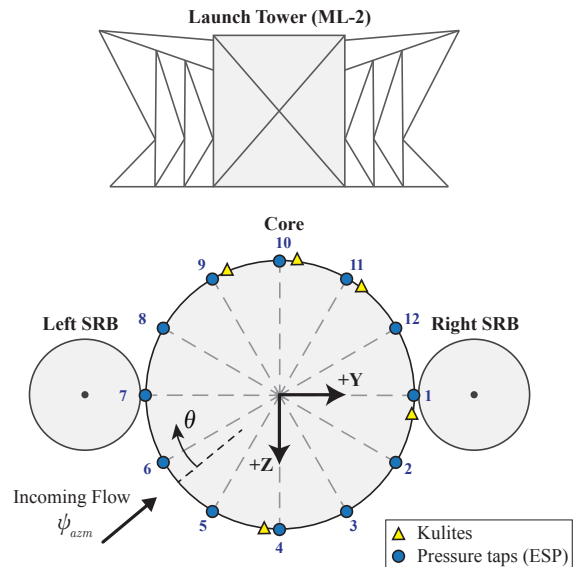

Fig. 7   Top-down view of the model showing the location of 12 pressure taps and 5 surface-mounted Kulites spaced 3° from the taps (ML-2 not to scale).

Fig. 8   Photograph of the ML-2 tiers showing Mini-45 load cells.

Fig. 9   Tier definitions and load cell locations in the ML-2 tower.

III. New Measurements and Instrumentation

A. Tower Section Loads

The tower was instrumented with eight ATI Mini-45 load cells mounted on a steel tower support, or strongback. Each load cell provided six-axis force and moment measurements for individual sections of the tower, which was divided into 10 tiers. It was not possible to instrument the lowest two tiers, and so load cells were installed in Tiers 3 - 10 and Tiers 1 and 2 were fixed to the launch platform. The individual tiers were 3D printed using filament impregnated with carbon fibers for increased strength and stiffness and include aluminum mounting plates to attach to the load cells, which are installed in cavities in the strongback. The tier features include replica pressure and electrical cables, personnel structures, cameras, and structural truss to a high degree of fidelity with the real-world tower for the most realistic estimate of aerodynamic loading on the tower. Figure 10 shows the global tower coordinate system and definitions of the individual forces and moments. It should be noted that the coordinate system and forces and moments match those of SLS vehicle and not typical building or tower aerodynamic force and moment coefficients.

Small metric gaps between the tiers were maintained to prevent fouling, but it was not feasible to monitor for fouling during the test. Instead, an assessment was conducted to manually load the tiers and measure the interference between towers. Typical results are shown in Fig. 11, with the loaded tier colored in red and the other (static) tiers shown in gray. During normal force loading of Tier 6, slight interference to Tier 5 and 7 were noted, but the magnitude is within acceptable levels.
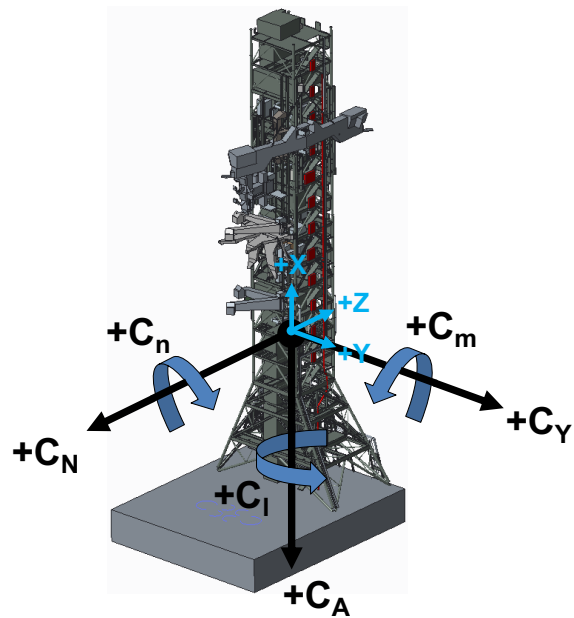
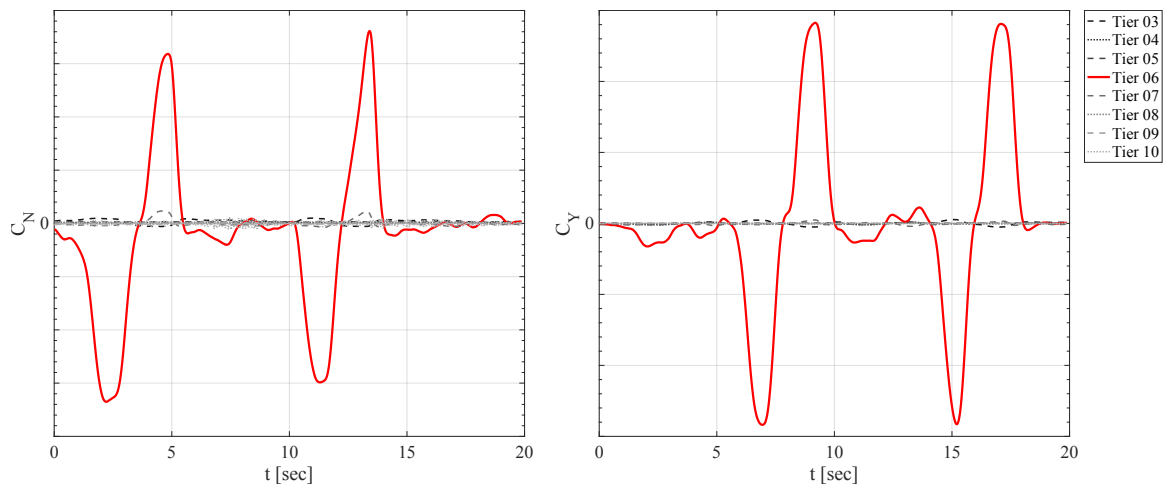**Fig. 10 Coordinate system for force and moment data for the ML-2 tower.**

Fig. 11 Normal and side force manual loading of Tier 6 and resulting interference with other tier load cells.

B. Unsteady Pressure

The pressure scanner used for measuring unsteady pressure was a TE Connectivity ESP-32HD module with a full scale range of 1 psid. 12 of the 32 available pressure scanner ports were connected to pressure taps on the model surface in an azimuthal ring at a single axial location on the nose of the B1B cargo vehicle. The tubing length was approximately 14 inches total, comprising 6 inches of stainless steel tubing, 8 inches of 0.040 inch inner diameter Tygon tubing, and an adapter to a short length (about 1/4 inch) of 0.065 inch inner diameter tubing to connect to the ESP module. Although the pressure ports are located approximately 2 core diameters (D) above the SRBs the outline of the SRBs are shown in Fig. 7 for reference.

The ESP sampling rate for each channel is 2,000 Hz for a duration of 6 seconds, resulting in 12,000 total samples. Since the signal is digitally multiplexed, no antialiasing filtering is applied during digitization. The ESP module does not sample individual channels simultaneously; instead, each subsequent port is sampled at 40 μs intervals within the 500 μs sampling period.

IV. Results and Discussion

The test results that are discussed here are only those which are unique to the present test. Contributions that overlap previous tests include the transition portion of flight, separate SRB force and moment measurements, and time-averaged surface pressures on the model. The focus will be on the distributed tower loading, flip-flopping flow state identification, and unsteady pressure measurements. All results are obtained at nominal flow conditions of $M_\infty = 0.18$ and dynamic pressure of 50 psf.

A. Tower Distributed Loads

In addition to the single global force and moment measurement on the tower structure, distributed loads indicate significant interaction with the wind direction, ψ_{azm}, and vehicle height with respect to the launch tower, h/L. It should be noted that these forces account only for the wind loads on the tower, while in reality, substantial loading on the structure from engine plume interactions will be experienced after liftoff for h/L greater than 0 that is not modeled here. An example of the loads with increasing h/L for the Block 1B Crew vehicle at $\psi_{azm} = 195°$, where the vehicle sits upstream of the ML-2, is shown in Fig. 12. The axial force coefficient (C_A) is aligned along the height of the tower with positive force pointing toward the launch platform (-X in Fig. 10). As the SLS vehicle lifts off, Tier 8 experiences positive axial force throughout the h/L range of 0.2 to 0.5, and Tier 7 experiences positive axial force at $h/L = 0.2$ and 0.25. Tier 6 shows positive axial force from $h/L = 0$ through 0.3 and again above 0.5. At $h/L = 0$, when the vehicle fully blocks the tower, most of the tiers except for 8, 9, and 10 show approximately zero normal force coefficient (C_N), then decrease as the vehicle blockage moves upward and the tower experiences the wind forces.

Side force (C_Y) is accentuated for upper tiers at low h/L because the incoming wind angle, ψ_{azm}, is equal to 195° and the nose of the vehicle strongly deflects the wind to strike the tower downstream of the vehicle. As vehicle elevation increases, side force diminishes when the vehicle shields the tier, for example, around $h/L = 0.4$ for Tier 10, and increases again once the tier becomes exposed again, which occurs near $h/L = 0.8$ for Tier 10. The distribution of tier forces by height means that vehicle elevation produces the strongest effect on the measurements at each tier, and the pattern observed at this incoming wind angle is largely dominated by the blockage of the SLS vehicle.

The forces and moments on individual tower tiers are also shown as a function of incoming wind angle, ψ_{azm}, at $h/L = -0.003$ in Fig. 13. At incoming wind angles of 0°/360°, the tower lies upstream of the SLS vehicle and the tower experiences high positive normal force (C_N). At $\psi_{azm} = 180°$, the tower tiers are almost totally shielded by the vehicle and lower tiers (3 - 6) are largely unaffected and experience nearly zero C_N, while higher tiers are affected by the incoming flow and experience negative normal force. Side force (C_Y) approaches minimum and maximum values at $\psi_{azm} = 90°$ and 270°, when the incoming wind is directed towards the sides of the ML-2. The effect of side force on individual tiers is lowest at Tier 3 and increases with elevation. Tier 10 sits above the vehicle at $h/L = -0.003$, and experiences the highest magnitude normal force and axial forces throughout the range of ψ_{azm} tested.

B. Multimodal Flow States

Since the data acquired during these tests are used to build static loads databases, instantaneous flow conditions were not explicitly monitored. Instead, as long as average values from the force balance and surface pressure remained relatively steady, the flow was assumed constant. Upon investigating repeat run behavior, discrepancies in normal force and side force were observed near $\psi_{azm} = 180°$ that could not be explained by instrumentation error or tunnel conditions.
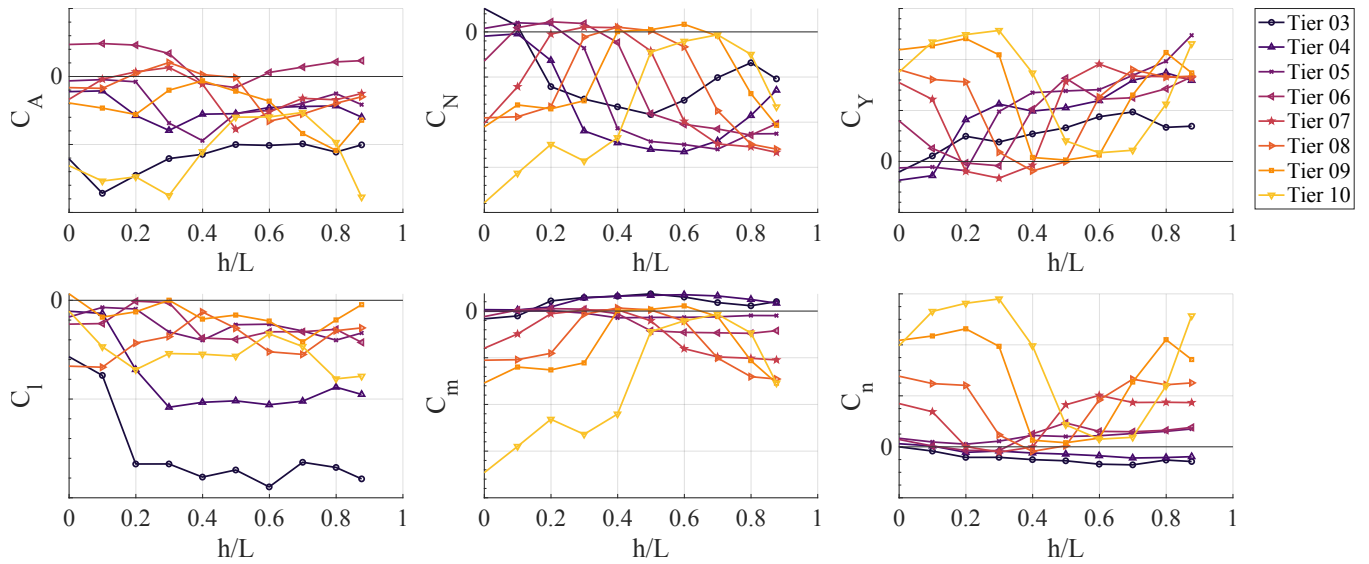
Fig. 12   Load results distributed throughout the tower at ψ_{azm} = 195°.
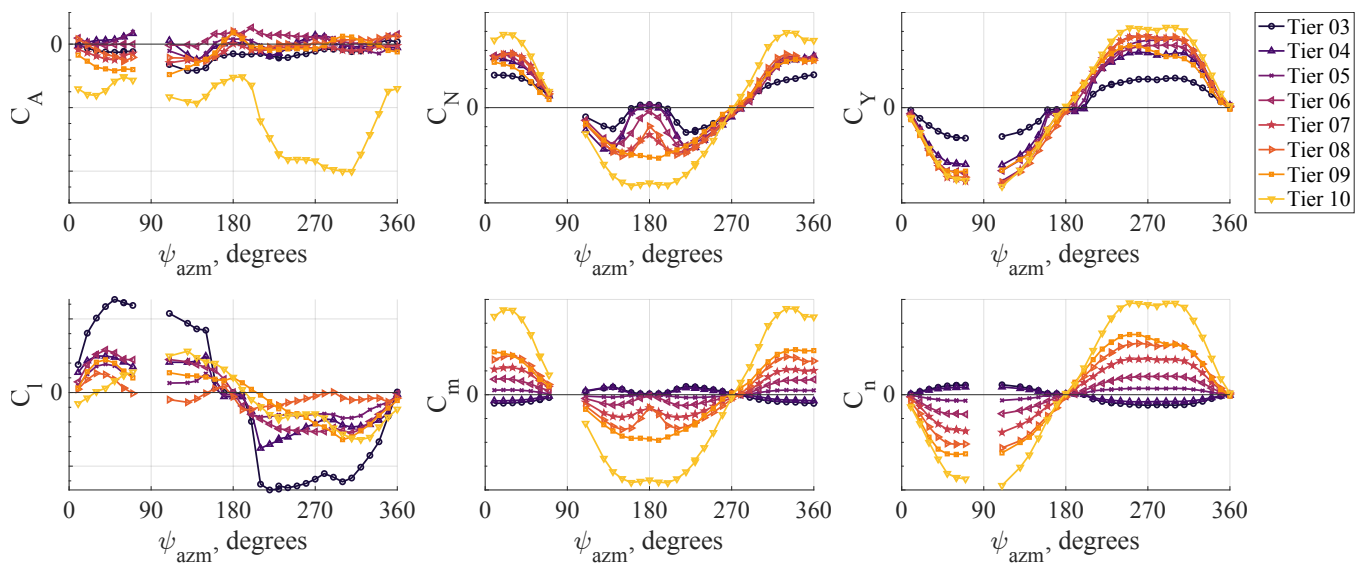

Fig. 13   Load results distributed throughout the tower at h/L = -0.003.

The differences manifested themselves in an apparently random fashion and occurred in both B1B crew and cargo liftoff configurations with and without the ML-2 present. One example in side force, C_Y, is shown in Fig. 14(a), where the specific range of ψ_{azm} values highlighted in blue were noted for poor repeatability. The pitching moment measured in the same tests also demonstrates poor agreement in the shaded region of Fig. 14(b). Although the differences may appear small, the poor agreement between in-test repeat measurements warranted additional analysis.

The measurements are averages of 8 seconds of data recorded when the tunnel conditions and model are stationary. Since these data are used to build static loads databases, this length of time is selected to average out turbulent or small periodic fluctuations and to ensure that the measured value is an accurate representation of the force or surface pressure that the vehicle experiences under specific conditions. After examining the time-varying or "frame" data shown in Fig. 15, it is apparent that an unsteady fluid dynamics phenomenon was responsible for the discrepant averages. Flow visualization using smoke flow and tufts revealed that a flip-flopping phenomenon was present in the gap flow between the SRBs and the core, and aperiodic switching between flow attached to the SRB surface and the core produced the rapid swings in side force and moments in Fig. 15. Although this is a well-known phenomenon for cylinders of similar sizes, the three-body geometry with wide differences in cylinder size has not been fundamentally investigated [11]. This discovery led to the implementation of a more complex loads database that accounts for the unpredictability of the flow states and resulting vehicle loads. More information on this investigation, including images of the smoke and tufts visualization, have been documented by Walker [12].
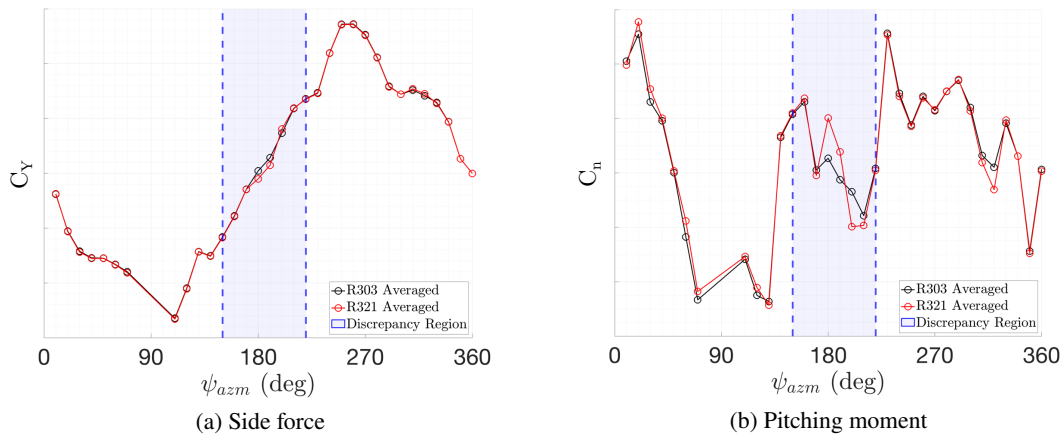

(a) Side force

(b) Pitching moment

Fig. 14   Runs demonstrating poor repeatability near ψ_{azm} = 160° - 200° for the B1B Crew vehicle.

C. Unsteady Pressure

Valuable insight into the flow physics observed in a wind tunnel test can be gained with measurements of unsteady pressure on the surface of the vehicle. As mentioned in Section II.D, a new variable, θ, is introduced to display the surface pressure with respect to the incoming flow direction such that $\theta = 0°$ always corresponds with the stagnation point of the flow, assuming the vehicle is a circular cylinder (see Fig. 7). This permits a more intuitive comparison when examining the flow physics at different incoming flow angles, since the nominal stagnation point defined by the incoming flow direction is always "clocked" to $\theta = 0°$. In addition to variations in ψ_{azm} and h/L, the flowfield differences at three vehicle and ML-2 configurations will be examined as well (see Fig. 4).

1. Pressure Intensity (σ)

The root-mean-squared pressure fluctuations at each measurement location are plotted as a 2-D contour plot with the incoming flow angle, ψ_{azm}, plotted on the abscissa and pressure sensor location, θ, on the ordinate axis. Each figure contains data from a full sweep of ψ_{azm} and represents 33 separate data acquisition test points. Plotting is limited ("clipped") to $\sigma = 0.25$ in order to provide a visually distinctive range and facilitate useful comparisons to cases with weaker unsteadiness. Figure 16 shows the distribution of pressure intensity for the configuration with the ML-2 and umbilicals retracted at h/L = -0.003, where the launch vehicle sits prior to liftoff. The strongest pressure fluctuations are noted at $\psi_{azm} = 180°$, where the ML-2 is immediately downstream of the vehicle. These peaks are located at
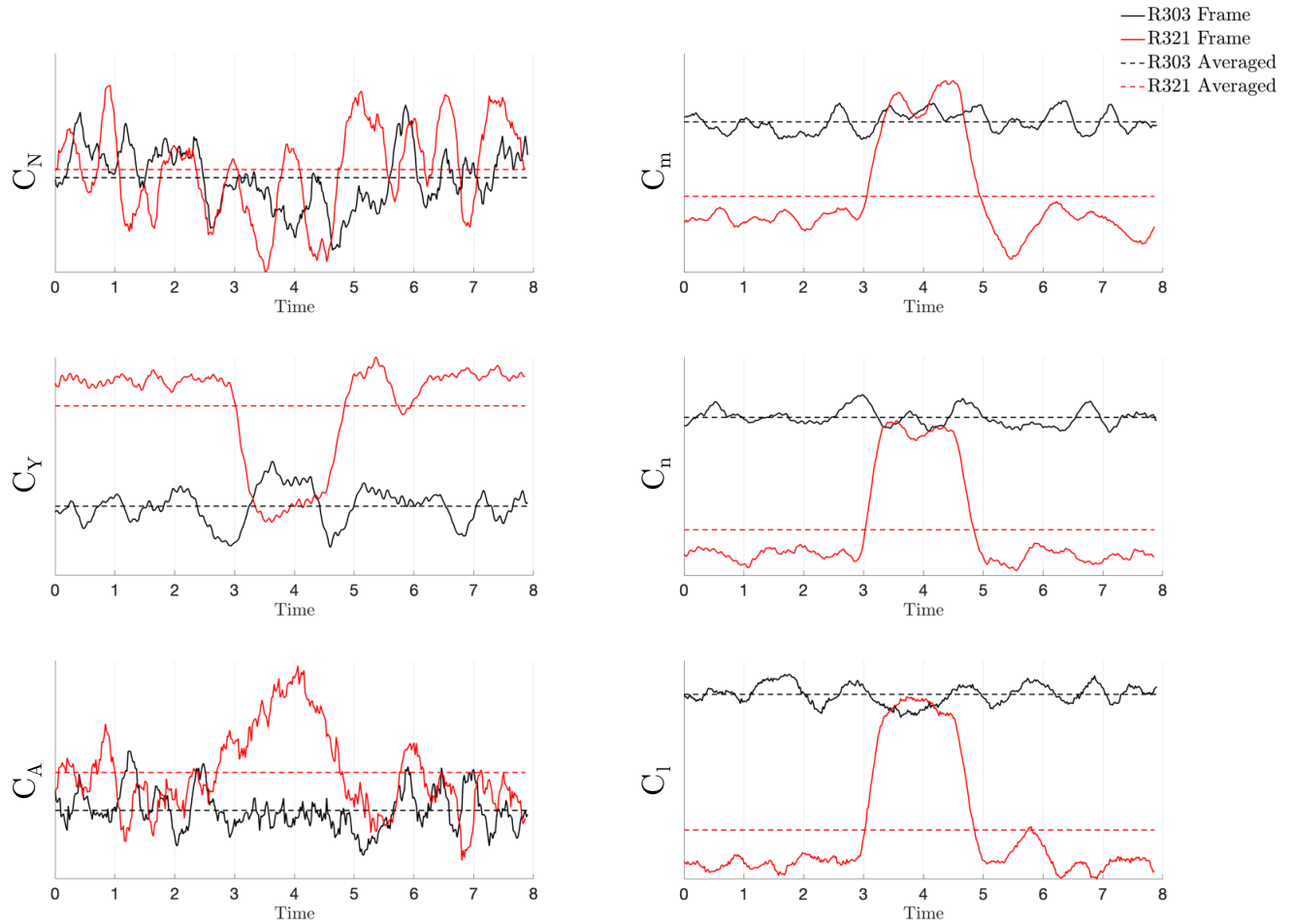
Fig. 15 Time trace of force and moment plots for the Block 1B Crew vehicle at ψ_{azm} = 200°.

$\theta = \pm 90°$, close to where separation would be expected on the sides of the vehicle [13]. The stagnation point of the flow near $\theta = 0°$ is visible as a region of very low pressure fluctuations. An additional region of relatively high pressure intensity is observed near $\theta = -120°$ at $\psi_{azm} = 330°$, where shedding from the tower is the likely source of relatively high unsteadiness on the surface of the vehicle. Near $\psi_{azm} = 0°$, unsteadiness is very low for all pressure ports because the flow passes through the ML-2 tower before reaching the vehicle, effectively reducing the fluctuations in the flowfield.

Since the ML-2 is not present in the vehicle-alone configuration (Fig. 17), negligible differences in σ are observed with variation in h/L. Figure 18 shows the pressure intensity for the configuration with the umbilicals deployed between the ML-2 and the SLS vehicle. The overall distribution of σ is very similar to the configuration with umbilicals retracted at h/L = -0.003 (Fig. 16). The strongest fluctuations appear at $\psi_{azm} = 180°$, but overall intensity is reduced compared to the case with umbilicals retracted, indicating that the wake interaction associated with highest unsteadiness is disrupted by the presence of the deployed umbilicals in the gap between the vehicle and tower.

2. Power Spectral Density (PSD)

The frequency distribution of pressure fluctuations can provide important information on the flow physics present for different model configurations and wind orientations. Peaks in spectral energy are clearly observed as bright yellow regions in Fig. 19, which shows the spatial distribution of surface pressure fluctuations at each frequency for the configuration with highest pressure fluctuations at $\psi_{azm} = 180°$ and h/L = -0.003. The bright yellow region at 22.5
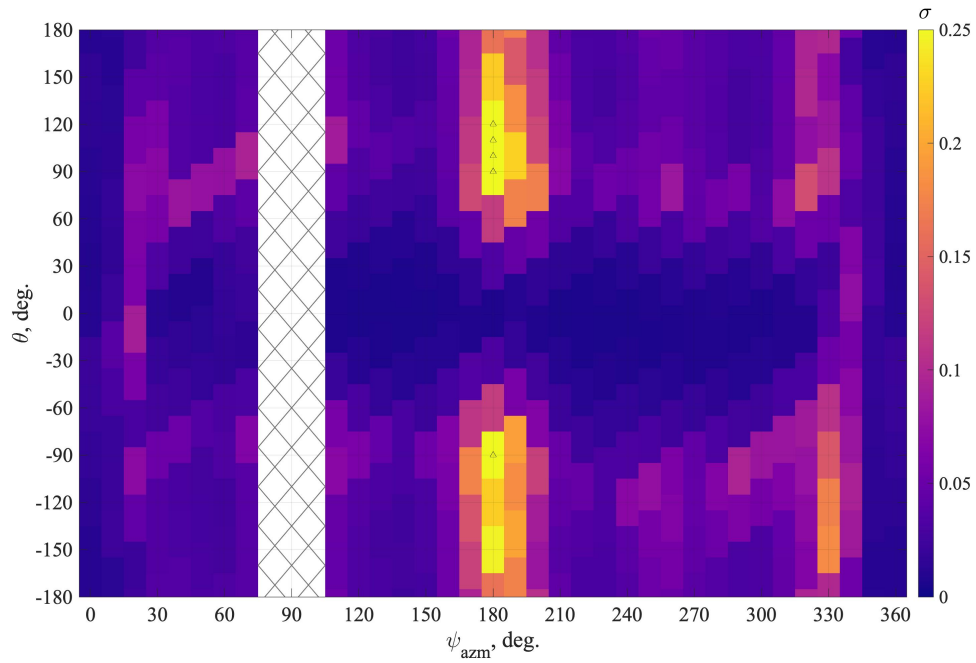
Fig. 16   Pressure intensity (σ) for the configuration with ML-2 (umbilicals retracted) at h/L = -0.003. Black triangles indicate levels of $\sigma > 0.25$.
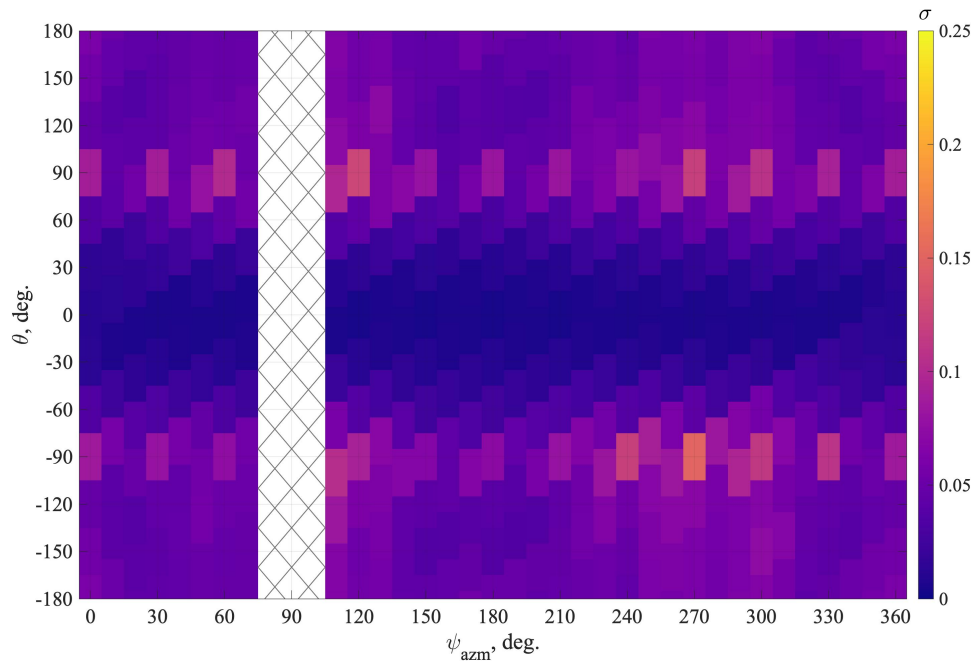

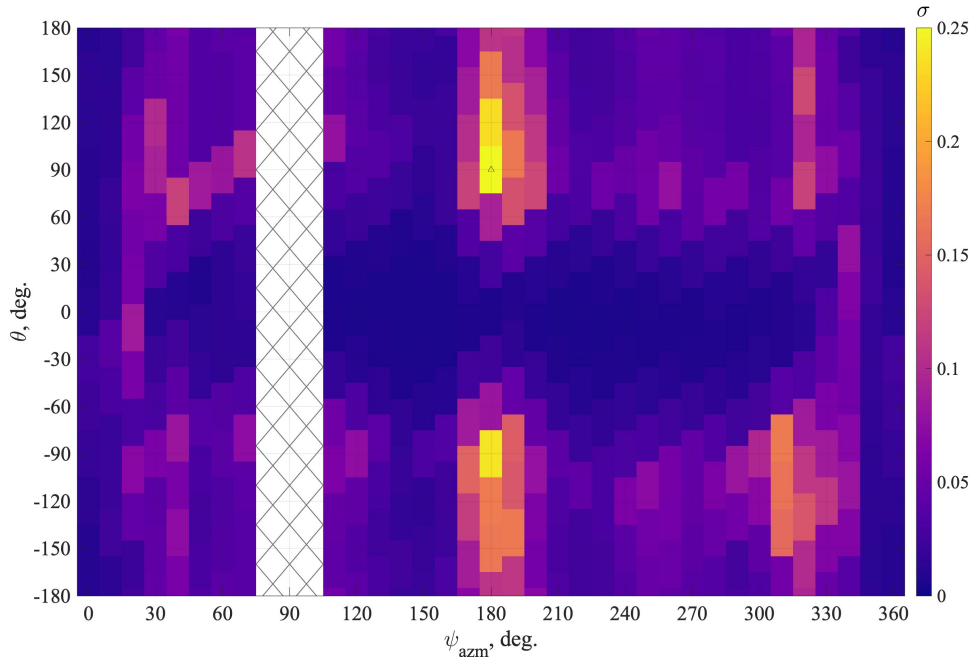**Fig. 17   Pressure intensity (σ) for the vehicle-alone configuration at h/L = -0.003.**

Fig. 18 **Pressure intensity (σ) for the configuration with ML-2 (umbilicals deployed) at h/L = -0.003. Black triangles indicate levels of σ > 0.25.**

Hz wraps around the circumference of the model (from -180° to +180°) and is especially strong at ±90°. Minimal fluctuations across all frequencies occur at the flow stagnation point, near $\theta = 0°$, and attached flow on the surface of the model produces low energy within high-frequency regions (above 200 Hz) between $\theta = \pm90°$ centered at 0°. The broadband distribution on the leeside of the vehicle, between $\theta = \pm120°$ wrapping around the top and bottom of the figure, indicates fully separated flow between the vehicle and tower.

The same flow conditions are shown in Fig. 20, where the tower includes the deployed umbilicals between the ML-2 and launch vehicle. The peak frequency increases to 27.5 Hz and overall intensity is lower than observed with umbilicals retracted, and apparent harmonics are also visible around 55 Hz and 82.5 Hz. Both configurations can be compared to experiments with only the launch vehicle (Fig. 21), with similar distribution in frequency to those with the ML-2 present. Strong fluctuations at $\theta = \pm90°$ indicate the onset of separation; fully separated flow behind the vehicle produces a broad distribution of frequencies up to the maximum resolvable frequency, 1 kHz. The most significant difference between the cases with and without the tower present is that no peak frequencies appear without the tower, suggesting that the strong fluctuations are a coupled effect created by a wake interaction between the vehicle and tower. It is not clear how the wake interaction, which occurs in the gap between the vehicle and tower, produces pressure fluctuations that are apparent in the attached flow at the front of the vehicle, between $\theta = \pm60°$.

The complex flowfield that exists in the wake interaction between two generic bluff bodies is difficult to predict from a fundamental physics perspective, let alone for complex geometries such as a cylindrical launch vehicle with protuberances and a truss structure. The PSD without the tower (Fig. 21) shows no coherent vortex shedding at any particular frequency when $\psi_{azm} = 180°$ when the two SRBs are perpendicular to the flow. The increase and tonal nature of the fluctuating pressure observed with blockage in the wake of the vehicle (Figs. 19 and 20) is a potential indication of resonant flow features occurring in the gap between two bodies, albeit at lower frequencies and at smaller gap spacings than observed in tandem cylinder studies in the subcritical flow regime, Re_D less than 2×10^5 [8]. The Strouhal number of the 22.5 Hz peak in Fig. 19 using the cylinder diameter D (St_D) equals 0.051, while the Strouhal number using the gap between the vehicle and the tower is 1.28 times higher (0.066) - neither of which appear physically meaningful in single or tandem cylinder flow studies. Treating the gap as a cavity and estimating Rossiter tones for the gap geometry yields expected frequencies in excess of 100 Hz [14], much higher than the fundamental frequencies observed. It is possible that separated shear layer excitation and acoustic resonance from the wake interaction with the tower are responsible for the strong pressure fluctuations that are felt upstream of flow separation on the vehicle surface, but the current measurements do not provide conclusive evidence of the underlying flow phenomena. Although surface
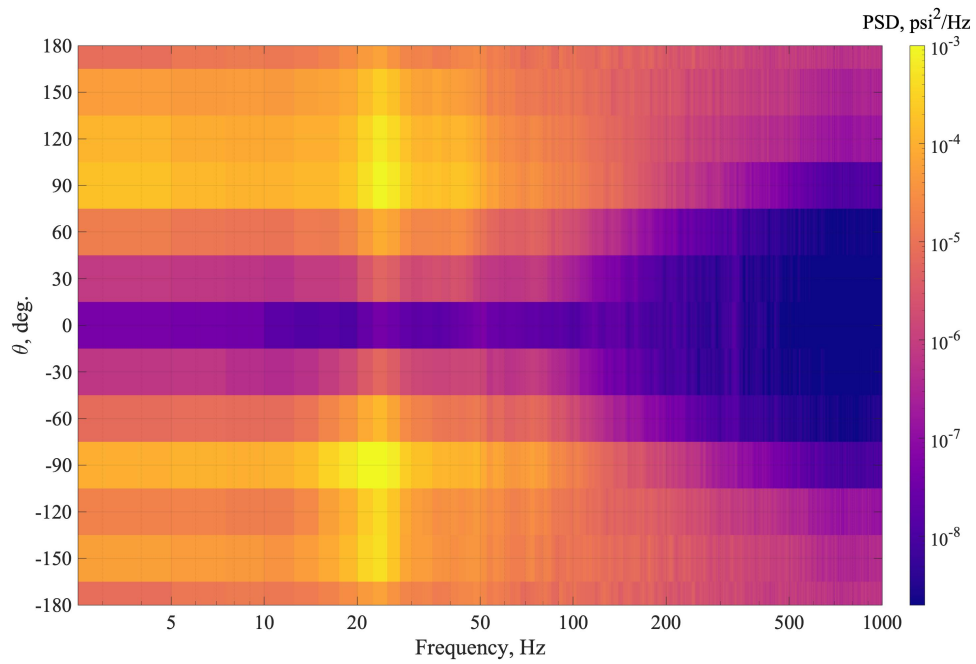
Fig. 19   Distribution of PSD for the configuration with ML-2 (umbilicals retracted) at ψ_{azm} = 180° and h/L = -0.003.
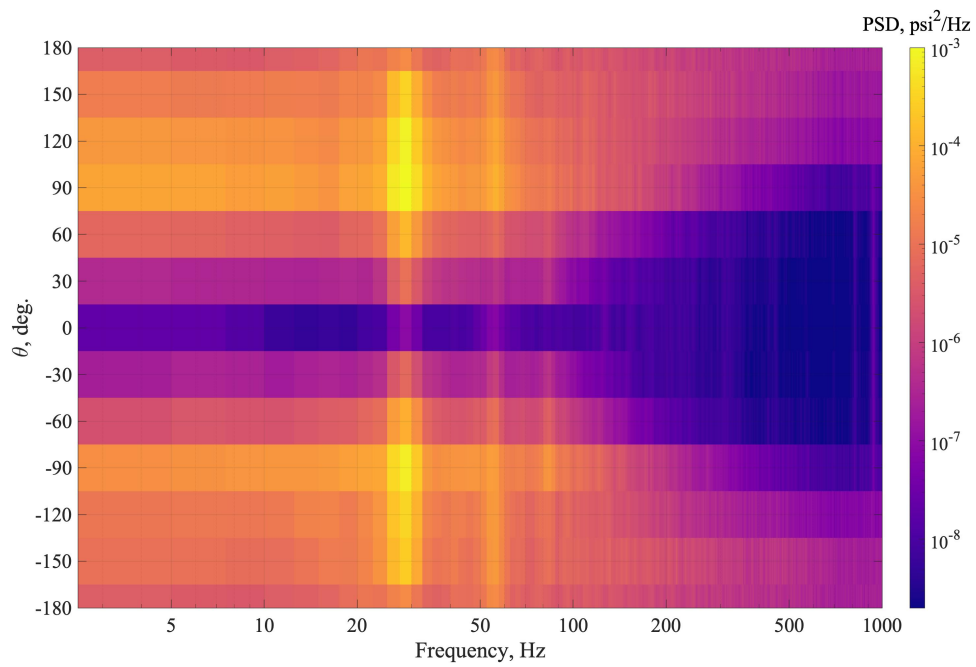

Fig. 20   Distribution of PSD for the configuration with ML-2 (umbilicals deployed) at ψ_{azm} = 180° and h/L = -0.003.
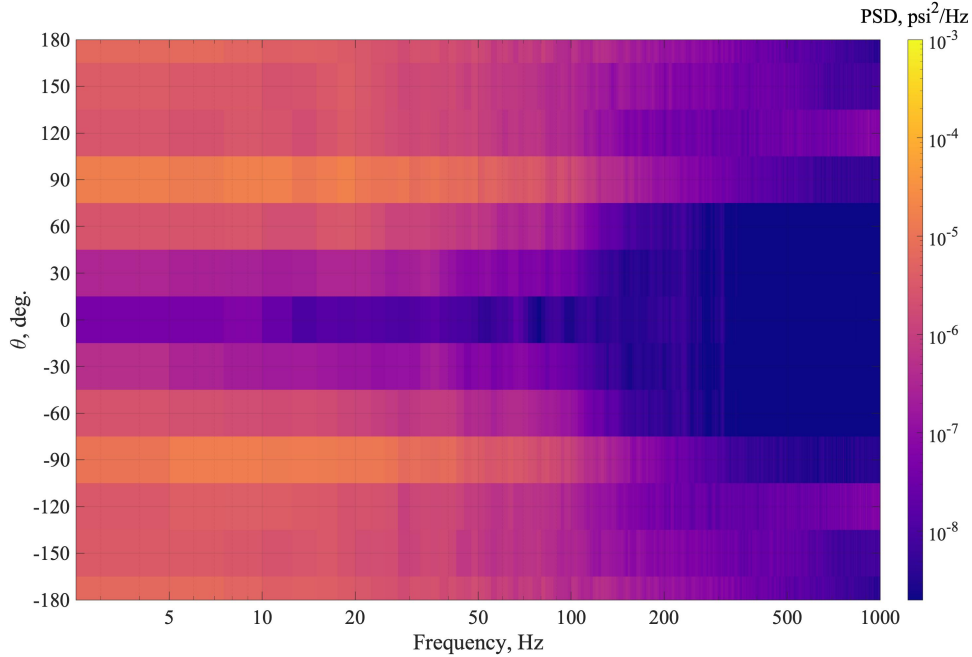
Fig. 21 Distribution of PSD for the vehicle-alone configuration at ψ_{azm} = 180° and h/L = -0.003.

pressure measurements are not sufficient for definitive characterization of the flow physics, additional off-body flowfield measurements are required to determine the mechanism driving the amplification in unsteady pressure.

3. High Resolution Case

A single case was selected for additional analysis specifically for unsteady pressure in the vehicle-alone configuration at a height of h/L = 0.5, which is approximately the center of the wind tunnel. While typical increments in ψ_{azm} were 10°, this test consisted of rotation increments of 1° from ψ_{azm} = 245° to 275°. The underlying assumption was that this could approximate a higher spatial resolution measurement, assuming that overall flow physics are not substantially different throughout the range of rotation. This requires that the measurement region is largely axisymmetric (ignoring SRB and protuberance effects). Although this assumption is not entirely correct, the geometry is predominantly cylindrical and the data are shown at 1° increments in θ. This results in some small discontinuities, which can be seen in the plot of pressure intensity in Fig. 22.

The pressure intensity σ centers around a minimum point at θ = 0°. There is a smooth increase in pressure unsteadiness leading to sharp peaks very close to ±90°, where the boundary layer separates. This is consistent with previous studies with rough cylinders in the transcritical Reynolds number range [13]. The two peaks are not symmetric, with greater unsteadiness noted at θ = -90° than +90°. This can be attributed to geometrical asymmetries on the SRB noses or other small protuberances on the vehicle core, or potentially to differences in grit application in the region. This can be compared to the pressure intensity plotted in Fig. 17, which is from a separate wind tunnel run and demonstrates consistent results. After the peak σ, the unsteadiness quickly falls to about half the peak amplitude on the leeward side of the vehicle, where the flow is fully separated. The pressure intensity associated with the separated flow is not fully converged with 6 seconds of acquisition, leading to the choppy appearance of the distribution of σ.

The PSD for this high spatial resolution case is plotted in Fig. 23. The highest amplitude signals, observed just above ±90°, include slight peaks near 32.5 Hz, which is equal to St_D = 0.075. The increased spatial resolution does not help determine how this fundamental frequency might be relevant to the global flow dynamics experienced by the vehicle, but it does highlight how sharp the transitions from an attached boundary layer with steadily increasing frequencies to fully separated flow, which encompasses pressure fluctuations up to the maximum resolvable frequency, 1 kHz. Although this additional test with small rotations does not reveal any unexpected features in the flowfield, it highlights how fortuitous the initial measurements were to capture the high unsteadiness at θ = ±90°; if the sensors were shifted by 5° in the original placement, this peak in unsteadiness would have been missed.
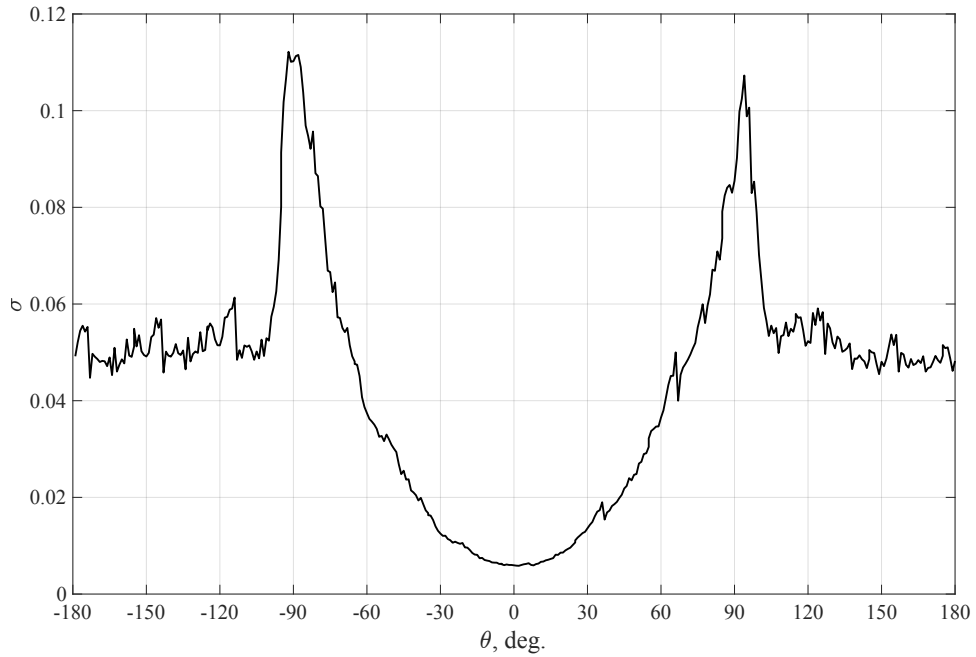
Fig. 22   Distribution of σ for the vehicle-alone configuration at ψ_{azm} = 245° to 275° and h/L = 0.5.
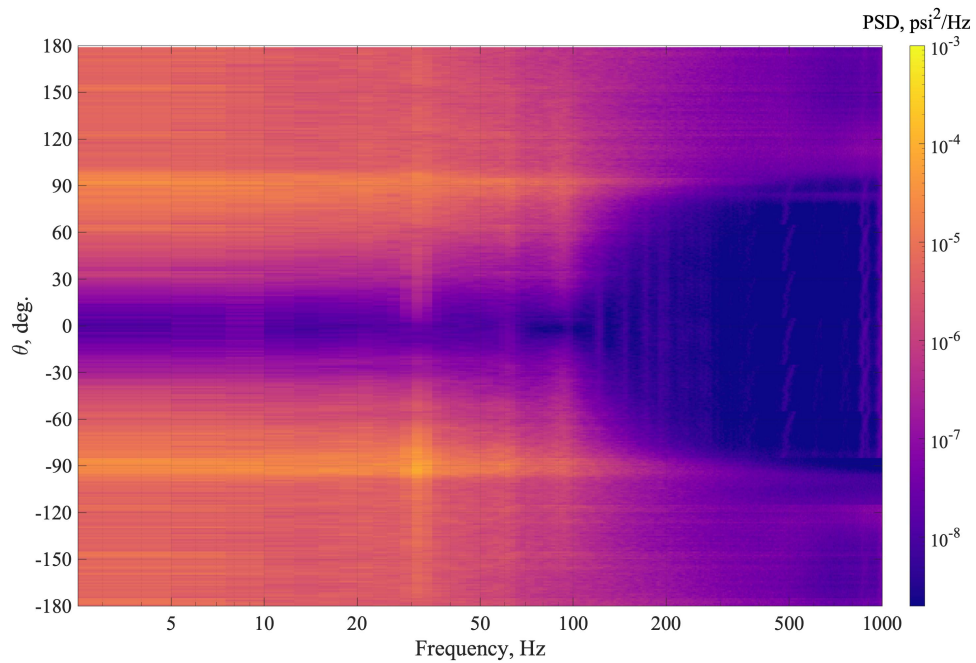

Fig. 23   Distribution of PSD for the vehicle-alone configuration at ψ_{azm} = 245° to 275° and h/L = 0.5.

V. Conclusions

The current study achieved the goals of providing aerodynamic data for the SLS Block 1B crew and cargo vehicles in the liftoff and transition flight environment and the ML-2 launch tower due to ground wind loads. The 1.75%-scale low-speed tests have become a vital component of database development for the SLS aerodynamics program, with continual improvements to testing capabilities and procedure. During the transition testing phase, aerodynamic

characteristics of the updated B1B cargo vehicle were successfully measured across angles of attack from -10° to 90° with 0° to 330° of roll, which covers all angles of attack and sideslip angles from 0° to 90°. Tower interference was characterized for both B1B crew and cargo vehicles at nearly 360° of incoming wind direction and a wide range of relative elevations of the launch vehicle with respect to the ML-2 launch tower to cover any expected ground winds scenario.

This test applied pertinent lessons learned during previous LOT tests and implemented new measurement techniques that provided distributed loads on the ML-2 and unsteady pressure measurement on the B1B cargo nose. The isolated tier measurements on the launch tower showed reasonable magnitudes and trends, as well as insight into the local effect that the vehicle produces as a function of height above the launch pad. The unsteady pressure signals measured using the ESP closely tracked the simultaneously acquired Kulite signal and validated the methodology to nearly 500 Hz. Unique unsteady flow physics were observed, and a possible resonance phenomenon present at incoming flow direction of 180° was documented. During testing, bifurcated flow states were observed in the liftoff orientation that produced poor repeats and flow visualization was conducted to better understand the flow mechanism responsible. These results will be used to develop higher fidelity databases for Block 1B vehicle configurations.

Acknowledgments

References

[1] Chan, D. T., Paulson, J. W., Shea, P. R., Toro, K. G., Parker, P. A., and Commo, S. A., "Aerodynamic Characterization and Improved Testing Methods for the Space Launch System Liftoff and Transition Environment," *AIAA Aviation 2019 Forum, AIAA Paper 2019-3398*, 2019.

[2] Pinier, J. T., Herron, A., and Gomez, R. J., "Advances in the Characterization of NASA' s Space Launch System Aerodynamic Environments," *AIAA Aviation 2019 Forum, AIAA Paper 2019-3397*, 2019.

[3] Shea, P. R., Pinier, J. T., Houlden, H., Favaregh, A., Hemsch, M. J., Dalle, D. J., Rogers, S. E., Meeroff, J., and Lee, H. C., "Ascent Aerodynamic Force and Moment Database Development for the Space Launch System," *AIAA Aviation 2019 Forum, AIAA Paper 2019-3298*, 2019.

[4] Capone, F. J., Paulson, J. W., and Erickson, G. E., "Liftoff and Transition Aerodynamics of the Ares I Launch Vehicle," *AIAA Journal of Spacecraft and Rockets*, Vol. 49, 2012, pp. 564 – 573.

[5] Pinier, J. T., Erickson, G. E., Paulson, J. W., Tomek, W. G., Bennett, D. W., and Blevins, J. A., "Space Launch System Liftoff and Transition Aerodynamic Characterization in the NASA Langley 14- by 22-Foot Subsonic Wind Tunnel," *AIAA SciTech 2015 Forum, AIAA Paper 2015-0775*, 2015.

[6] "NASA SLS Configurations," https://www.nasa.gov/sites/default/files/atoms/files/sls_lift_capabilities_configurations_04292020_woleo.pdf, 2020. Accessed October 26. 2021.

[7] Gentry Jr, G. L., Quinto, P. F., Gatlin, G. M., and Applin, Z. T., "The Langley 14- by 22-foot Subsonic Tunnel: description, flow characteristics, and guide for users," NASA TP 3008, National Aeronautics and Space Administration, 1990.

[8] Neuhart, D. H., and McGinley, C. B., "Free-Stream Turbulence Intensity in the Langley 14- by 22-Foot Subsonic Tunnel," NASA TP 213247, National Aeronautics and Space Administration, 2004.

[9] Smith, S., "Aerial of NASA Langley Research Center Wind Tunnel," https://images.nasa.gov/details-LRC-2013-00135, 2012. Accessed November 2, 2022.

[10] Mears, L. J., Shea, P. R., Collins, J. G., Walker, M. A., Langston, S. L., Pinier, J. T., Nikoueeyan, P., Perry, M., Strike, J., Wimpenny, B., Hind, M., and Naughton, J. W., "Unsteady Pressure Acquisition on the 1.75% Scale SLS Block 1B Cargo Liftoff Configuration," NASA TM-20220002633, National Aeronautics and Space Administration, 2022.

[11] Wu, G., Lin, W., and Du, X., "On the flip-flopping phenomenon of two side-by-side circular cylinders at a high subcritical Reynolds number of 1.4×10^5," *Physics of Fluids*, Vol. 32, 2020, pp. 1–24.

[12] Walker, M. A., Pinier, J. T., Shea, P. R., Collins, J. G., Mears, L. J., Lee, M. W., and Pomeroy, B. W., "Experimental Identification of Bistable Flow States on the Space Launch System at Liftoff Conditions," *AIAA Aviation 2022 Forum, AIAA Paper 2022-3665*, 2022.

[13] Shih, W. C. L., Wang, C., Coles, D., and Roshko, A., "Experiments on Flow Past Rough Circular Cylinders at Large Reynolds Numbers," *Journal of Wind Engineering and Industrial Aerodynamics*, Vol. 49, 1993, pp. 351 – 368.

[14] Rossiter, J. E., "Wind-Tunnel Experiments on the Flow over Rectangular Cavities at Subsonic and Transonic Speeds," R. and M. No. 3438, Aeronautical Research Council, 1964.